Chinese Journal of Catalysis 81 (2026) 185–194

available at www.sciencedirect.com

ScienceDirect

journal homepage: www.sciencedirect.com/journal/chinese-journal-of-catalysis

Article

Bipyridine-integrated bisoxazole-based donor-acceptor covalent organic framework for enhanced photocatalytic H_2O_2 synthesis

Jiaping Lu [a,b,1], Chao Lin [a,b,1], Chao Li [c,1], Hongjie Shi [a,b], Nengyi Liu [a,b], Wandong Xing [a,b,*], Sibo Wang [a,b,*], Guigang Zhang [a,b], Teng-Teng Chen [c,*], Xiong Chen [a,b,*]

[a] *State Key Laboratory of Chemistry for NBC Hazards Protection, College of Chemistry, Fuzhou University, Fuzhou 350116, Fujian, China*

[b] *State Key Laboratory of Photocatalysis on Energy and Environment, Key Laboratory of Advanced Carbon-Based Functional Materials, College of Chemistry, Fuzhou University, Fuzhou 350116, Fujian, China*

[c] *Department of Chemistry, The Hong Kong University of Science and Technology, Kowloon 999077, Hong Kong (SAR), China*

ARTICLE INFO

Article history:
Received 8 July 2025
Accepted 15 September 2025
Available online 5 February 2026

Keywords:
Covalent organic frameworks
Donor-acceptor
Photocatalysis
H_2O_2 production
Oxygen reduction reaction

ABSTRACT

The deliberate integration and precise arrangement of electron donor (D) and acceptor (A) moieties within the crystalline lattices of covalent organic frameworks (COFs) represent a sophisticated strategy to optimize charge separation and electron transfer processes, thereby enhancing photocatalytic efficiency. Herein, we report the rational design and synthesis of two novel bisoxazole-based D-A type COFs, designated as Bpy-COF and Bph-COF. These frameworks incorporate identical acceptor units but are distinguished by their unique donor motifs, enabling a comparative evaluation of their structural and functional properties. The results reveal that Bpy-COF, which incorporates bipyridyl (Bpy) donor moieties, exhibits superior photocatalytic H_2O_2 production performance compared to Bph-COF, potentially related to its broader light response range and increased availability of reactive sites. Furthermore, the coplanar and conjugated nature of the Bpy groups facilitates efficient charge separation and migration, thereby accelerating the two-electron oxygen reduction reaction critical to H_2O_2 synthesis. This study affirms the effectiveness of manipulating the structural components of COF photocatalysts, propelling new insights for the design and synthesis of high-performance catalysts.

1. Introduction

Hydrogen peroxide (H_2O_2), recognized as an environmentally benign and versatile oxidant [1], is integral to numerous applications, including bleaching [2], disinfection [3], waste water treatment [4], fuel cells [5], and others [6]. However, the predominant industrial method for H_2O_2 production, the anthraquinone oxidation process, is hindered by substantial energy demands and the generation of toxic by-products [7]. Consequently, there is a pressing need for sustainable and en-

* Corresponding author. E-mail: xwd@fzu.edu.cn (W. Xing), sibowang@fzu.edu.cn (S. Wang), tengtengchen@ust.hk (T. Chen), chenxiong987@fzu.edu.cn (X. Chen).

[1] Contributed equally to this work.

This work was supported by the National Key R&D Program of China (2021YFA1502100), the Natural Science Foundation of Fujian Province (2024J01238), the National Natural Science Foundation of China (22572031, 52201006, 22172029), the 111 Project (D16008), the start-up fund (R9874) from HKUST, Early Career Scheme (26311224), the General Research Fund (16312125) from the Research Grants Council of Hong Kong, the Young Elite Scientists Sponsorship Program by the China Association for Science and Technology (CAST) (2023QNRC001), and the open research fund of Key Laboratory of Precision and Intelligent Chemistry.
https://doi.org/10.1016/S1872-2067(25)64864-9

ergy-efficient alternatives. Photocatalysis emerges as a promising green technology, characterized by its cleanliness, cost-effectiveness, and sustainability [8–10]. Recent advancements have identified various semiconductors, such as TiO_2 [11,12], $BiVO_4$ [13,14], polymeric carbon nitride [15–17], metal organic frameworks (MOFs) [18,19], conjugated microporous polymers (CMPs) [20,21,22], and covalent organic frameworks (COFs) [23–28], as effective catalysts for photocatalytic oxygen reduction reactions (ORR) to produce H_2O_2. Among these, two-dimensional (2D) COFs, constructed from planar molecular building blocks, are advantageous due to their abundant catalytic sites, extended conjugated systems, tunable bandgap structures, and customizable porosity, positioning them as highly promising candidates for efficient H_2O_2 photocatalysis [29–52].

Within the context of COF photocatalysts, the rapid carrier recombination and inefficient photogenerated charge transport are the main factors limiting photocatalytic performance [53–57]. The large Coulomb force within COF skeletons restricts the separation efficiency of photogenerated electron-hole pairs. To address these challenges, the incorporation of donor-acceptor (D-A) configurations has been explored as a strategy to reduce exciton binding energy (E_b) and enhance charge separation efficiency [58–64]. Additionally, the integration of bipyridine (Bpy) units, known for their excellent electronic properties and planar geometry, has been widely adopted in COF design to extend conjugation without increasing the molecular length of building blocks [65]. Moreover, the lone pair of electrons on the N species of the Bpy structure can promote rapid protonation under photoexcitation, which helps to form 1,4-endoperoxides and enables an efficient two-electron ORR pathway for H_2O_2 production [66,67].

Against this backdrop, in this study, we introduce two novel D-A COFs, Bpy-COF and Bph-COF, constructed using 4,4′,4″,4‴-(benzo[1,2-d:4,5-d′]bis(oxazole)-,4,6,8-tetrayl)tetra phenylamine (BBO-NH_2) as the acceptor units, paired with bipyridine (Bpy) and biphenyl (Bph) as donor units, respectively (Fig. 1(a)). Through a synergistic combination of experimental and computational analyses, we demonstrate that Bpy-COF exhibits markedly superior photocatalytic performance for H_2O_2 production compared to Bph-COF. The enhanced conjugation provided by Bpy units not only mitigates exciton binding through optimized D-A interactions but also facilitates interlayer charge transfer. Additionally, the incorporation of nitrogen atoms in Bpy-COF extends the material's light absorption range, and modulates active sites, effectively lowering the energy barrier for H_2O_2 photosynthesis. These findings underscore the critical role of molecular design in advancing photocatalytic systems and highlight the transformative potential of heterocyclic motifs in enhancing the functionality of COFs for sustainable H_2O_2 production.

2. Experimental

2.1. COF synthesis

Bpy-COF was synthesized by the Schiff base reaction of BBO-NH_2 and [2,2′-bipyridine]-5,5′-dicarbaldehyde (Bpy-CHO). The mixture was reacted at 393.15 K for 72 h through solvothermal method. The resulting mixture was extracted and dried to obtain Bpy-COF powder. The synthetic method of Bph-COF is similar to Bpy-COF, while

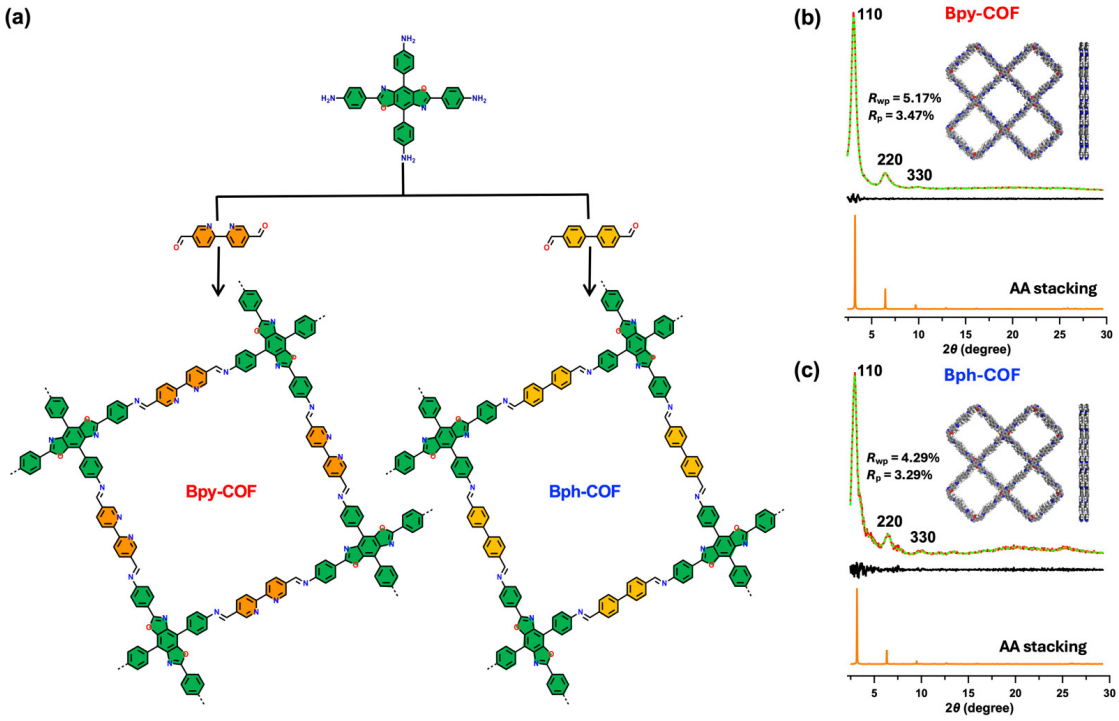

Fig. 1. (a) Synthetic routes for Bpy-COF and Bph-COF. The PXRD profiles of Bpy-COF (b) and Bph-COF (c): experimental (red), Pawley refined (dotted green), the difference (black), the simulated curves for eclipsed AA stacking mode (orange) (Insets are the top view (left) and side view (right) of the AA packing mode of Bpy-COF (b) and Bph-COF (c), Grey: C atoms; blue: N atoms; red: O atoms; white: H atoms).

4,4'-biphenyldicarb-oxaldehyde (Bph-CHO) is used as the donor building block instead of Bpy-CHO (Fig. 1(a)). Elemental analysis revealed that the compositions of both COFs closely matched their theoretical values, confirming the successful preparation of the targeted frameworks (Table S1).

2.2. Methods

^{1}H Nuclear magnetic resonance (NMR) spectra of all monomers were carried out on a Bruker AVANCE III-400MHz NMR spectrometer. The crystalline phases and morphology of the COFs were characterized by powder X-ray diffraction (PXRD Rigaku MiniFlex 600), and scanning electron microscopy (SEM, Nova Nano 230). Structural information was obtained employing Fourier transform infrared (FTIR, Thermo Nicolet Magna 670), solid-state ^{13}C cross polarization-magic angle spinning (CP/MAS) NMR (Bruker Advance III 500) as well as X-ray photoelectron spectroscopy (XPS, Thermo ESCALAB250). Elemental analysis (EA) was conducted on Elementary Vario MICRO cube. The porosity of the photocatalysts was assessed by nitrogen sorption isotherms at 77 K after degassing, which is conducted on Micromeritics ASAP 2460. Absorption spectra were recorded on a PerkinElmer Lambda Ultraviolet-visible (UV-vis) spectrophotometer. Temperature-dependent photoluminescence (PL) and fluorescence lifetimes of samples were estimated on a FS/FL920 time resolved fluorescence spectrometer. Electron paramagnetic resonance (EPR) measurements were performed on Bruker model A300 spectrometer and photoelectrochemical properties of the samples were studied on a BioLogic VSP-300 electrochemical system.

2.3. Photocatalytic H_2O_2 production experiments

10 mg of COF photocatalyst, 20 mL of pure H_2O or a mixed solvent of H_2O/benzyl acohol (BA) (9/1 in vol%) were charged into a 50 mL Schlenk reactor, dispersed and stirred with a magnetic stirrer. Under the atmosphere of O_2, the mixture was irradiated with a 420 nm LED monochromatic light for 1 h. Collect samples from the solution at fixed 1-h intervals. After dilution, 0.02 mol L^{-1} $Ti(SO_4)_2$ was employed as a color reagent. The absorbance at 410 nm was monitored using a UV/Vis spectrophotometer and the H_2O_2 concentration was determined.

3. Results and discussion

3.1. Structural and electronic characterizations

The successful synthesis of these two COFs was confirmed through comprehensive spectroscopic and structural analyses. FTIR spectroscopy (Fig. S1) revealed a characteristic stretching vibration peak at 1580 cm^{-1}, corresponding to the C=N imine bond, indicating successful condensation in both COFs. This was corroborated by ^{13}C solid-state NMR spectra (Fig. S2), which provided further evidence of imine bond formation. XPS elucidated the elemental composition and chemical states of the COFs. The survey spectra (Fig. S3(a)) confirmed the presence of carbon (C), nitrogen (N), and oxygen (O) in both frameworks. High-resolution C 1*s* spectra (Fig. S3(b)) displayed five distinct peaks, corresponding to C=C, C–CH=C, C=C–O, C=C–N, and N=C–O bonds, reflecting the diverse chemical environments within the COF structures. The N 1*s* spectra (Fig. S3(c)) exhibited a peak near 399 eV, indicative of C=N bonds and complete consumption of amino groups. Similarly, the O 1*s* spectra (Fig. S3(d)) showed peaks at 534 eV (oxazole) and 531 eV (adsorbed water), confirming the complete reaction of aldehyde groups. Thermogravimetric analysis (Fig. S4) demonstrated that both materials possessed good thermal stability under a nitrogen atmosphere, retaining structural integrity up to temperatures exceeding 250 °C.

PXRD analysis (Figs. 1(b), (c)) demonstrated the high crystallinity of both COFs. Bpy-COF (Fig. 1(b)) exhibited a prominent diffraction peak at 3.02°, with additional peaks at 6.47° and 9.67°, corresponding to the (110), (220), and (330) crystal planes, respectively. Comparable diffraction patterns were observed for Bph-COF (Fig. 1(c)), indicating similar structural ordering. Simulations based on an AA stacking model closely matched the experimental PXRD patterns (Figs. 1(b), (c) insets and Figs. S5, S6), confirming that both COFs adopt an AA stacking arrangement. The corresponding unit cell parameters are summarized in Tables S2, S3. Morphological characterization by SEM and TEM revealed that both COFs consisted of nanoscale particles (Fig. S7). High-resolution TEM (HRTEM) images displayed distinct lattice fringes with spacings consistent with the (001) plane, further confirming their good crystallinity. Elemental mapping demonstrated a uniform distribution of elements throughout the particles, corroborating the successful synthesis of the materials (Fig. S8).

Nitrogen sorption isotherms measured at 77 K (Fig. S9(a)) revealed type IV behavior for both COFs, indicating the presence of mesoporous structure within the COFs. The Brunauer-Emmett-Teller (BET) surface areas were determined to be 777 and 351 m^2 g^{-1} for Bpy-COF and Bph-COF, respectively. The higher surface area of Bpy-COF is likely caused by the smaller intramolecular dihedral angle of Bpy units compared to Bph motifs, resulting in reduced lattice distortion in Bpy-COF. Pore size distributions, calculated using non-local density functional theory (NLDFT), indicated a dominant pore size of approximately 2.95 nm for both COFs (Fig. S9(b)). Given that hydrophilicity may affect photocatalytic H_2O_2 generation, water contact angle measurements (Fig. S10) were performed, showing that Bpy-COF (24.4°) possesses markedly higher surface wettability than Bph-COF (42.7°). Water vapor adsorption isotherms (Fig. S11) further confirmed the superior hydrophilicity of Bpy-COF, which exhibited substantially greater vapor uptake across the measured pressure range. This enhanced hydrophilicity is expected to promote more efficient photocatalytic H_2O_2 production.

The thermodynamic feasibility of photocatalytic H_2O_2 production was assessed through electronic structure analyses. UV-vis diffuse reflectance spectroscopy (DRS) (Fig. 2(a)) revealed a broader spectral response for Bpy-COF, with an absorption edge at 600 nm, compared to 500 nm for Bph-COF. Corresponding bandgap energies (E_g) were calculated as 2.09

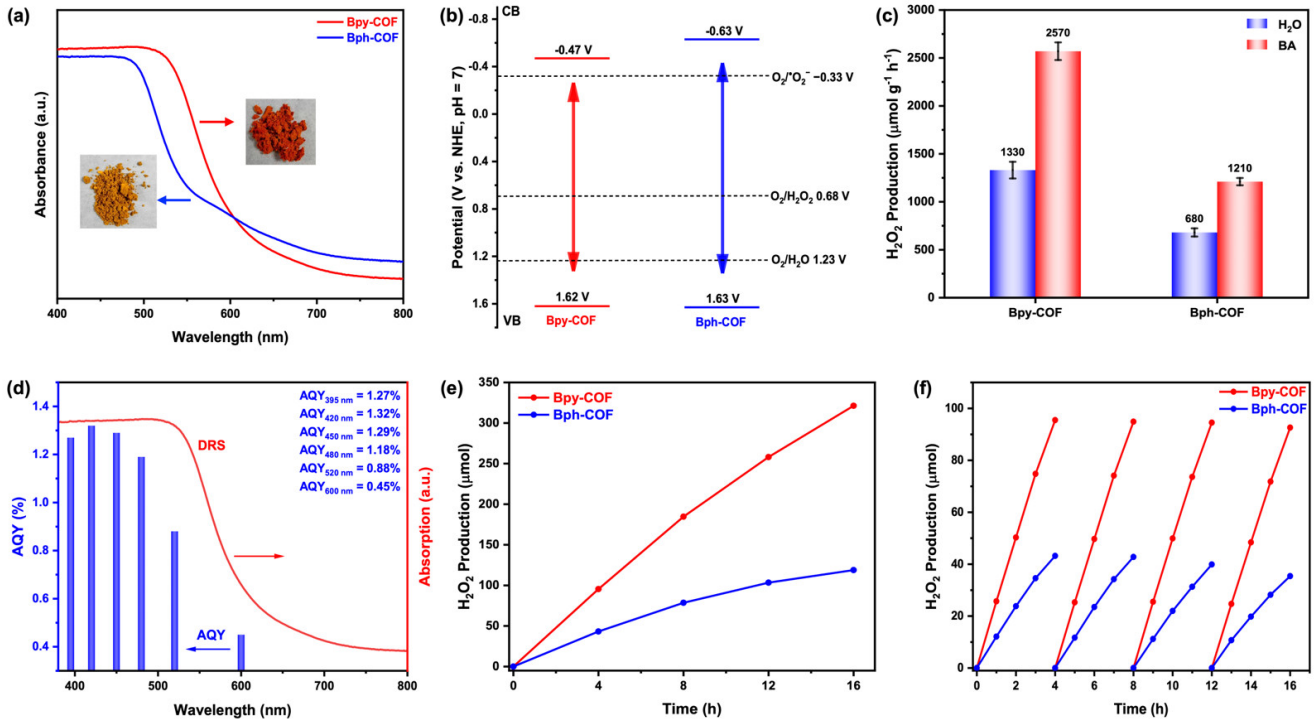

Fig. 2. (a) UV-vis DRS of COFs in the solid state (insets are the optical images of Bph-COF and Bpy-COF). (b) Band alignments of COFs. (c) The reaction photocatalytic activities of COFs within 1 h. (d) The wavelength-dependent of the AQYs of Bpy-COF. (e) Long-term photocatalytic activities of COFs within a 16-h period. (f) Recycling photocatalytic activity of COFs for four 4-h cycles times (total 16 h).

and 2.26 eV for Bpy-COF and Bph-COF, respectively (Fig. S12), consistent with the trends predicted by density functional theory (DFT) calculations (Fig. S13). A subsequent Mott-Schottky (M-S) analysis (Fig. S14) enabled the identification of the flat band potentials for both COFs, suggesting their *n*-type semiconductor characteristics. The conduction band (CB) energy levels for Bpy-COF and Bph-COF were then estimated to be −0.47 and −0.63 eV (*vs.* normal hydrogen electrode (NHE), pH = 7), respectively. Using the equation $E_{VB} = E_{CB} + E_g$, the valence band (VB) energies were calculated as 1.62 and 1.63 eV (*vs.* NHE, pH = 7) for Bpy-COF and Bph-COF, respectively. These results enabled the construction of energy band diagrams (Fig. 2(b)) [68], demonstrating that both COFs possess suitable band alignments to thermodynamically drive oxygen reduction reactions (ORR) for H_2O_2 production. The enhanced light absorption and optimized electronic structure of Bpy-COF suggest its superior potential for efficient photocatalytic performance.

3.2. *Photocatalytic H_2O_2 production*

The photocatalytic activity of Bpy-COF and Bph-COF for H_2O_2 production was evaluated under controlled illumination using a 420 nm LED light source (details see experimental section). In pure water, both COFs demonstrated notable photocatalytic capabilities, with Bpy-COF achieving a H_2O_2 production rate of 1330 μmol h^{-1} g_{cat}^{-1} outperforming Bph-COF, which yielded 680 μmol h^{-1} g_{cat}^{-1} (Fig. 2(c)). It is worth noting that the design of the H_2O/BA biphasic system was designed such that the COF photocatalyst remains primarily dispersed and active in the BA (organic) phase. In this configuration, photogenerated holes oxidize BA to benzaldehyde within the organic phase, while photogenerated electrons drive the oxygen reduction reaction (ORR) at the H_2O/BA interface, producing H_2O_2. Due to its hydrophilicity, the generated H_2O_2 rapidly diffuses into the aqueous phase. This spatially separated biphasic architecture not only stabilizes the photocatalyst and suppresses agglomeration and deactivation, but also enhances the activity of Bpy-COF by enabling rapid product removal and sustained BA supply. As a result, Bpy-COF achieves an H_2O_2 production rate of 2570 μmol h^{-1} g_{cat}^{-1}, more than twice that of Bph-COF (1210 μmol h^{-1} g_{cat}^{-1}), placing it among the most active COF-based photocatalysts reported to date (Table S4). These results highlight the superior photocatalytic efficiency of Bpy-COF, attributable to the incorporation of Bpy moieties, which enhance electronic conjugation and charge dynamics compared to Bph units. Given that H_2O_2 formation and decomposition occur concurrently, kinetic analyses (Fig. S15) reveal that Bph-COF exhibits a faster decomposition rate, whereas Bpy-COF delivers a higher steady-state yield owing to its greater formation rate and slower decomposition kinetics.

The efficiency of light utilization was quantified through apparent quantum yield (AQY) measurements (Figs. 2(d) and S16). At 420 nm, Bpy-COF exhibited an AQY of 1.32%, substantially higher than the 0.56% recorded for Bph-COF, underscoring Bpy-COF's enhanced ability to harness light energy for photocatalytic H_2O_2 production. Under AM 1.5G simulated sunlight, the solar-to-chemical conversion (SCC) efficiencies of Bpy-COF and Bph-COF were approximately 0.036% and 0.021%, respectively. Long-term stability and recyclability were assessed through extended illumination (Fig. 2(e)) and

cycling experiments (Fig. 2(f)), which revealed a linear relationship between H_2O_2 yield and illumination time for both COFs, indicative of consistent and robust photocatalytic activity over prolonged periods. Post-photocatalysis structural analyses further confirmed the stability of the COFs. FTIR spectroscopy (Fig. S17) demonstrated that the core chemical structures of both COFs remained intact, highlighting their chemical stability under photocatalytic conditions. However, PXRD analysis (Fig. S18) indicated a partial reduction in crystallinity for both COFs, likely due to exfoliation of their layered structures during photocatalysis. XPS analysis (Fig. S19) revealed that 50.7% of nitrogen atoms in Bpy-COF were protonated (-NH^+) after cyclic testing, substantially higher than the 24.9% observed for Bph-COF. This elevated protonation density is attributed to the synergistic effect of the dual nitrogen sites in the Bpy unit, which generate specific oxygen activation sites.

3.3. Mechanism exploration

To elucidate the charge separation kinetics in Bpy-COF and Bph-COF, temperature-dependent photoluminescence (PL) spectra were recorded and analyzed (Figs. 3(a) and S20). A progressive quenching of PL intensity with increasing temperature was observed over the range of 15-300 K. The relationship between the integrated PL intensity and temperature was subsequently fitted to the Arrhenius equation, $I(T) = I_0 / (1 + A\exp(-E_b/k_BT))$ [69–71], yielding E_b values of approximately 55 and 64 meV for Bpy-COF and Bph-COF, respectively. These results suggest that charge separation is more favorable in Bpy-COF. Steady-state PL spectra and time-resolved PL spectroscopy of both COFs provided insights into the electron-hole separation efficiency. The steady-state PL emission intensity significantly attenuated from Bph-COF to Bpy-COF (Fig. 3(b)), signifying suppressed charge recombination in Bpy-COF. Time-resolved PL spectroscopy (Fig. S21) further supported this, with average charge carrier lifetimes of 1.20 ns for Bpy-COF and 0.37 ns for Bph-COF. The prolonged lifetime in Bpy-COF enhances the availability of photogenerated charges for photocatalytic processes, underscoring the efficacy of Bpy moieties in mitigating electron-hole recombination. Additionally, Bpy-COF exhibited lower photoresistance (Fig. S22) and a stronger photocurrent response (Fig. S23) compared to Bph-COF, confirming superior charge transfer kinetics driven by Bpy functionalization [72–76]. The photovoltaic and Kelvin probe force microscopy (KPFM) measurements (Figs. S24–S26) revealed enhanced photoresponse characteristics and a stronger surface potential for Bpy-COF relative to Bph-COF, confirming improved photogenerated charge separation efficiency and a more pronounced built-in electric field. Collectively, these factors underpin the superior photocatalytic performance of Bpy-COF.

Transient absorption spectroscopic (TAS) studies were

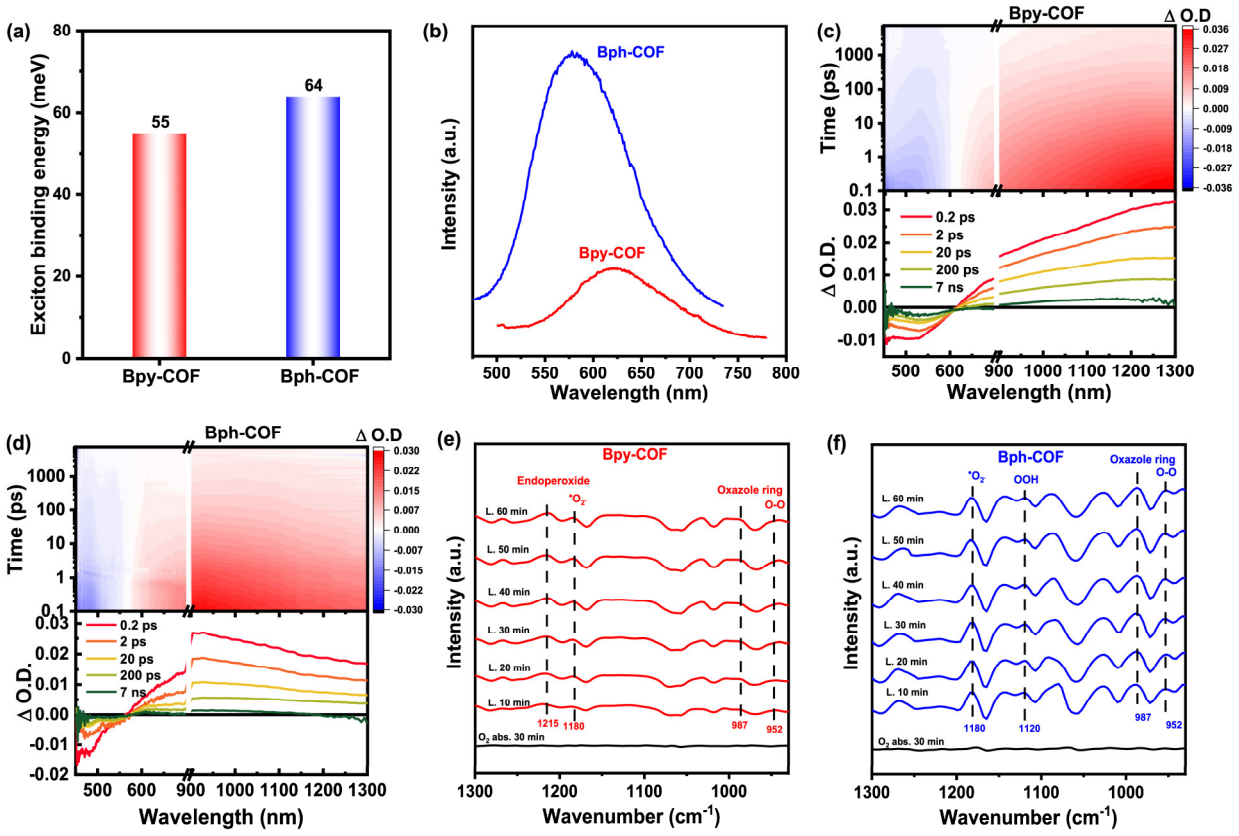

Fig. 3. Estimated exciton binding energy value (a)s and steady-state photoluminescence spectra (b) of COFs (λ_{ex} = 475 nm). The complete transient absorption (TA) surface and the corresponding TA spectra at selected pump-probe time delays of Bpy-COF (c) and Bph-COF (d) following 435 nm excitation. The break in the region of 700–900 nm is due to the data being recorded in two separate experiments (450–700 nm and > 900 nm). *In-situ* DRIFTS acquired over different illumination times for the Bpy-COF (e) and Bph-COF (f) photocatalytic systems (1283–933 cm^{-1}), respectively.

performed to investigate exciton dissociation dynamics in both Bpy-COF and Bph-COF (See SI for more details). Upon 435 nm excitation, initial TA spectra of both COFs exhibited broad negative signals with minima at ~530 nm (Bpy-COF) and ~480 nm (Bph-COF), respectively (Figs. 3(c), (d)). These features correspond to ground-state bleach (GSB) at the band edges, consistent with their steady-state absorption spectra (Fig. 2(a)). Notably, a weak and short-lived negative signal at ~550 nm emerged at ~0.2 ps exclusively in Bph-COF, which was assigned to stimulated emission (SE) based on the PL spectra and time-resolved PL data (Figs. 3(b) and S21).

In Bpy-COF, the broad GSB underwent a progressive blue shift with increasing time delays, indicating gradual generation of SE that spectrally overlapped the GSB. This behavior suggests more efficient charge separation in Bpy-COF, which prolongs the lifetime of photogenerated carriers by delaying charge recombination. Both materials displayed broad excited-state absorption (ESA) spanning the visible to near-infrared region (~600–1300 nm). Kinetic traces monitored at ESA and GSB maxima both revealed extended photogenerated excited state lifetimes in the sample of Bpy-COF (Fig. S27), demonstrating that enhanced donor-acceptor interactions promote charge separation efficiency. This leads to improved charge utilization and higher photocatalytic activity.

DFT calculations of the highest occupied molecular orbital (HOMO) and lowest unoccupied molecular orbital (LUMO) levels (Fig. S28) revealed that both COFs exhibited spatially separated delocalized characteristics, forming a D-A structure. This configuration minimizes charge carrier recombination, consistent with the low E_b values observed for both COFs [77]. Furthermore, DFT analysis of dihedral angles between donor units showed 0.97° for Bpy-COF (Fig. S29) and 35.43° for Bph-COF (Fig. S30). The near-planar geometry of Bpy-COF enhances π-conjugation, facilitating both intralayer and interlayer charge transfer through improved π-electron cloud overlap [78], thereby boosting photocatalytic performance.

The mechanistic pathways for H_2O_2 production were investigated through control experiments conducted under varying atmospheres (Fig. S31), confirming that H_2O_2 generation is oxygen-dependent and proceeds via an ORR pathway [79–82]. It is generally accepted that H_2O_2 may potentially be generated through either an indirect continuous two-step single-electron reduction or a direct one-step two-electron reduction route [83–88]. EPR measurements with 5,5-dimethyl-1-pyrroline N-oxide (DMPO) as a spin-trapping agent revealed distinct signals corresponding to superoxide radicals ($^{\bullet}O_2^-$) in both COFs (Fig. S32), whereas no signals attributable to hydroxyl radicals ($^{\bullet}OH$) were detected (Fig. S33). These findings indicate that the system exhibits high selectivity toward H_2O_2 production with negligible byproduct formation. Notably, the addition of Tiron, a $^{\bullet}OOH$ scavenger, significantly inhibited H_2O_2 production in Bph-COF but had minimal impact on Bpy-COF (Fig. S34). This suggests that Bph-COF primarily follows a two-step single-electron reduction pathway, while Bpy-COF employs both this pathway and a direct one-step two-electron reduction route. To further probe the ORR reaction pathways in photocatalytic H_2O_2 production, isotope labeling experiments using $^{18}O_2$ were conducted (Fig. S35). The results demonstrated that, following photocatalytic decomposition of the generated H_2O_2, $^1O_2$ was clearly detected by MnO_2, confirming that H_2O_2 was indeed produced through the photocatalytic reduction of oxygen.

To verify the specific role of the nitrogen atom, we designed and synthesized Fpy-COF, constructed using a structurally simplified 4-(5-formylpyridin-2-yl)benzaldehyde (a substituted biphenyl) as the building block, which was reacted with BBO-NH_2 via a Schiff base condensation. Comprehensive characterization, including PXRD, FTIR, and nitrogen sorption measurements, confirmed its high crystallinity and mesoporous structure (Figs. S36–S38). Under identical photocatalytic conditions, both in a pure water system and a water/BA biphasic system, the H_2O_2 production rates followed the order of Bph-COF < Fpy-COF < Bpy-COF (Fig. S39). This systematic trend strongly supports the critical contribution of the nitrogen atom in these COF materials toward enhancing photocatalytic H_2O_2 generation.

Furthermore, in situ diffuse reflectance infrared Fourier-transform spectroscopy (DRIFTS) was used to identify the intermediates involved in the photocatalytic H_2O_2-generation process in real time (Figs. 3(e), (f), and S40). In a steam-saturated O_2 environment without illumination, both COFs exhibited IR signals at 1614, 1457, and 987 cm^{-1} (Figs. 3(e), (f), and S40), corresponding to the C=N, benzene ring, and oxazole motifs, respectively. Bpy-COF additionally showed signals at 1558, 1538, and 1519 cm^{-1} (Fig. S40(a)), attributed to protonated C=NH^+ groups formed by N atoms in imine, oxazole, and Bpy units binding H^+. In contrast, Bph-COF, lacking pyridine units, displayed only the 1558 and 1538 cm^{-1} signals (Fig. S40(b)). This observation suggests that the N atoms on the COFs bind with H^+ prior to the reaction. Upon illumination, both COFs exhibited new IR signals at 952 and 1180 cm^{-1} (Figs. 3(e)–(f)), corresponding to O–O bonds and superoxide radicals, respectively. Furthermore, Bpy-COF exhibited an additional IR signal at 1180 cm^{-1} (Fig. 3(e)), indicative of an endoperoxide intermediate, with signal intensities increasing with illumination time. These findings confirm that Bph-COF relies on a two-step single-electron reduction, while Bpy-COF supports both this pathway and a one-step two-electron reduction.

To discern the binding mode of $^{\bullet}OOH$ as reaction intermediate with the reactive N atoms within the COFs, we employed DFT theoretical calculations to stimulate the process while also tracking the change of Gibbs free energy (Figs. 4(a), (b)) using implicit solvation models. In situations where the N atom in the COFs directly absorbs $^{\bullet}OOH$, the resultant energy barrier is 0.41 eV. Alternatively, when the N atom initially absorbs H^+, followed by $^{\bullet}OOH$, the energy barrier shrinks significantly to 0.14 eV, thus presenting lower hindrance to the reaction. Give the above outcomes, a plausible two-step single-electron reaction mechanism was proposed. Firstly, the holes (h^+) generated by photoexcited COFs react with the sacrificial agent, culminating in the release of H^+. Thereafter, H^+ interacts with the N atoms of COFs, creating a protonated NH^+ unit. Concurrently, the O_2 adsorbed on the NH^+ unit is reduced by the electrons (e^-) gener-

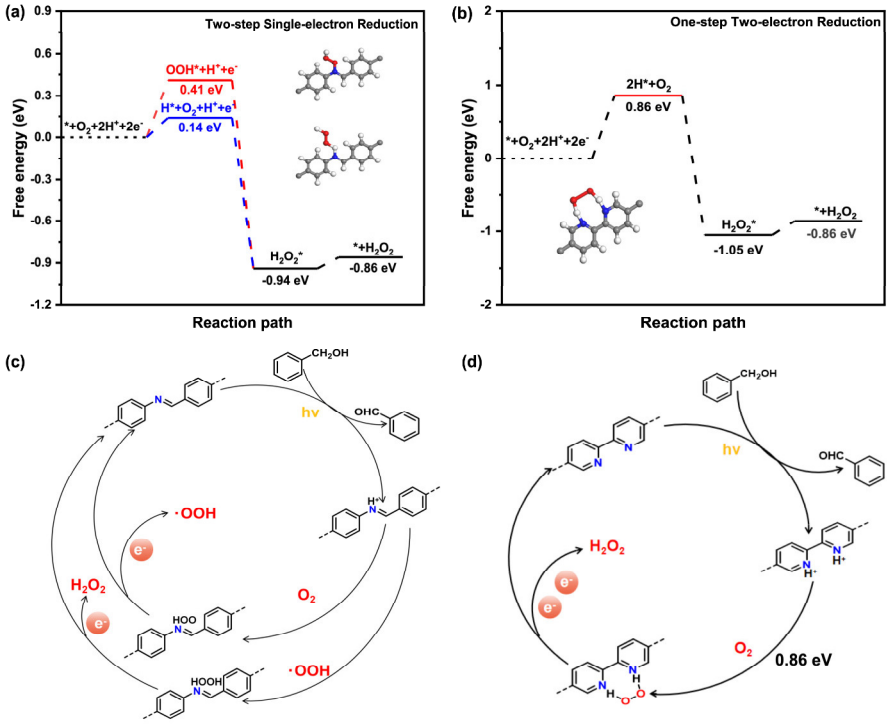

Fig. 4. DFT-calculated Gibbs free energy (Δ*G*, eV) profiles using implicit solvation models for photocatalytic H_2O_2 production by two-step single-electron reduction route (a) and one-step two-electron reduction route (b). Proposed mechanism for the photocatalytic H_2O_2 production by two-step single-electron reduction route (c) and one-step two-electron reduction route (d).

ated by photoexcited COFs to afford •OOH. Subsequently, •OOH is transferred and fixed to another NH^+ unit and then reduced by e^- to yield H_2O_2 (Fig. 4(c)). Conversely, due to the presence of the Bpy unit, the unique one-step two-electron reduction route of Bpy-COF does not rely on the intermediate •OOH. Initially, the N atoms of bipyridine interact with H^+, resulting in the formation of a protonated bipyridine motif ($BpyH^+$), which subsequently adsorbs O_2 and yields a 1,4-endoperoxide intermediate (N-H-O-O-H-N). H_2O_2 is ultimately produced via a $2e^-$ reduction pathway (Fig. 4(d)). Thus, Bpy functionalization not only optimizes reactive sites but also lowers reaction energies by enabling a dual-pathway mechanism, significantly enhancing photocatalytic H_2O_2 production.

4. Conclusions

In summary, we have successfully conceived two D-A COF photocatalysts with appropriate electronic band structures to produce H_2O_2 in this study. The establishment of a D-A structure leads to an improvement in the separation of photoexcited charges in COFs, enabling a study into the impact of different conjugated motifs on the photocatalytic performance of COFs. Notably, Bpy-COF exhibited a H_2O_2 production rate more than twice that of Bph-COF in a biphasic system, underscoring the pivotal role of Bpy units in boosting photocatalytic efficiency. Comprehensive experimental and theoretical analyses revealed that the integration of nitrogen-containing Bpy moieties imparts multiple advantages to Bpy-COF. First, the Bpy units broaden the spectral response range and introduce distinct reactive sites, facilitating efficient light absorption and catalysis. Additionally, the extended π-conjugation in Bpy-COF accelerates charge separation and interlayer charge transport, as evidenced by its lower exciton binding energy, higher photocurrent response, and reduced charge transfer resistance compared to Bph-COF. These attributes collectively contribute to Bpy-COF's superior photocatalytic performance. This work validates the efficacy of molecular engineering through strategic structural unit modulation in COF-based photocatalysts, illuminating new insights into the design and synthesis high-performance photocatalysts.

Acknowledgments

The authors acknowledge Beijing PARATERA Tech Co., Ltd. for providing access to high-performance computing resources that significantly contributed to the research results reported in this paper.

Electronic supporting information

Supporting information is available in the online version of this article.

References

[1] K. Oka, H. Nishide, B. Winther-Jensen, *Adv. Sci.*, **2021**, 8, 2003077.
[2] Y. Wu, J. Wu, F. Yang, C. Tang, Q. Huang, *Polymers*, **2019**, 11, 776.
[3] R. Wang, M. Shi, F. Xu, Y. Qiu, P. Zhang, K. Shen, Q. Zhao, J. Yu, Y. Zhang, *Nat. Commun.*, **2020**, 11, 4465.
[4] D. Zheng, G. Zhang, Y. Hou, X. Wang, *Appl. Catal. A*, **2016**, 521, 2–8.
[5] Y. Yamada, M. Yoneda, S. Fukuzumi, *Energy Environ. Sci.*, **2015**, 8,

Graphical Abstract

Chin. J. Catal., 2026, 81: 185–194 doi: 10.1016/S1872-2067(25)64864-9

Bipyridine-integrated bisoxazole-based donor-acceptor covalent organic framework for enhanced photocatalytic H_2O_2 synthesis

Jiaping Lu, Chao Lin, Chao Li, Hongjie Shi, Nengyi Liu, Wandong Xing *, Sibo Wang *, Guigang Zhang, Teng-Teng Chen *, Xiong Chen *
Fuzhou University;
The Hong Kong University of Science and Technology

A bipyridyl-group-anchored bisoxazole-based donor-acceptor type covalent organic framework, namely Bpy-COF, is proposed to realize facilitated photocatalytic H_2O_2 production. Experimental and theoretical outcomes verify that Bpy-COF experiences promoted exciton dissociation, suppressed charge recombination, accelerated charge transfer, and distinct reactive sites, and thus achieving boosted photocatalytic performance.

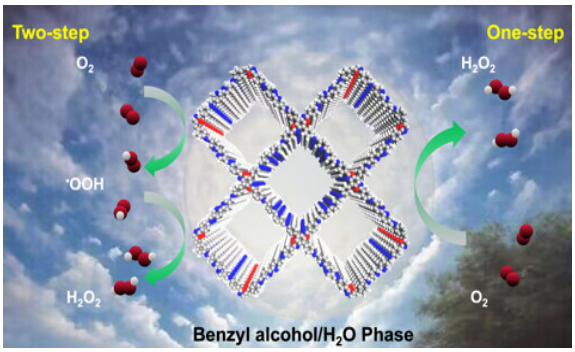

1698–1701.
[6] Y. Xiang, W. Dong, P. Wang, S. Wang, X. Ding, F. Ichihara, Z. Wang, Y. Wada, S. Jin, Y. Weng, H. Chen, J. Ye, *Appl. Catal. B*, **2020**, 274, 119096.
[7] N. Abutaha, A. Hezam, F. A. Almekhlafi, A. M. N. Saeed, K. Namratha, K. Byrappa, *Appl. Surf. Sci.*, **2020**, 527, 146893.
[8] G. Zhang, Z.-A. Lan, X. Wang, *Angew. Chem. Int. Ed.*, **2016**, 55, 15712–15727.
[9] Q. Wang, K. Domen, *Chem. Rev.*, **2020**, 120, 919–985.
[10] Y. Fang, Y. Hou, X. Fu, X. Wang, *Chem. Rev.*, **2022**, 122, 4204–4256.
[11] D. Tsukamoto, A. Shiro, Y. Shiraishi, Y. Sugano, S. Ichikawa, S. Tanaka, T. Hirai, *ACS Catal.*, **2012**, 2, 599–603.
[12] Y. Shiraishi, S. Kanazawa, D. Tsukamoto, A. Shiro, Y. Sugano, T. Hirai, *ACS Catal.*, **2013**, 3, 2222–2227.
[13] H. Hirakawa, S. Shiota, Y. Shiraishi, H. Sakamoto, S. Ichikawa, T. Hirai, *ACS Catal.*, **2016**, 6, 4976–4982.
[14] K. Fuku, R. Takioka, K. Iwamura, M. Todoroki, K. Sayama, N. Ikenaga, *Appl. Catal. B*, **2020**, 272, 119003.
[15] H. Ou, P. Yang, L. Lin, M. Anpo, X. Wang, *Angew. Chem. Int. Ed.*, **2017**, 56, 10905–10910.
[16] Z. Wei, M. Liu, Z. Zhang, W. Yao, H. Tan, Y. Zhu, *Energy Environ. Sci.*, **2018**, 11, 2581–2589.
[17] B. Feng, Y. Liu, K. Wan, S. Zu, Y. Pei, X. Zhang, M. Qiao, H. Li, B. Zong, *Angew. Chem. Int. Ed.*, **2024**, 63, e202401884.
[18] Y. Zhao, Y. Liu, Z. Wang, Y. Ma, Y. Zhou, X. Shi, Q. Wu, X. Wang, M. Shao, H. Huang, Y. Liu, Z. Kang, *Appl. Catal. B*, **2021**, 289, 120035.
[19] Y. Kondo, Y. Kuwahara, K. Mori, H. Yamashita, *Chem*, **2022**, 8, 2924–2938.
[20] Z. Luo, X. Chen, Y. Hu, X. Chen, W. Lin, X. Wu, X. Wang, *Angew. Chem. Int. Ed.*, **2023**, 62, e202304875.
[21] Q. Hao, Y. Tao, X. Ding, Y. Yang, J. Feng, R.-L. Wang, X.-M. Chen, G.-L. Chen, X. Li, H. OuYang, X. Hu, J. Tian, B.-H. Han, G. Zhu, W. Wang, F. Zhang, B. Tan, Z.-T. Li, D. Wang, L.-J. Wan, *Sci. China Chem.*, **2023**, 66, 620–682.
[22] S. Wang, Z. Xie, D. Zhu, S. Fu, Y. Wu, H. Yu, C. Lu, P. Zhou, M. Bonn, H. I. Wang, Q. Liao, H. Xu, X. Chen, C. Gu, *Nat. Commun.*, **2023**, 14, 6891.
[23] S. Chai, X. Chen, X. Zhang, Y. Fang, R. S. Sprick, X. Chen, *Environ. Sci. Nano*, **2022**, 9, 2464–2469.
[24] L. Zhai, Z. Xie, C.-X. Cui, X. Yang, Q. Xu, X. Ke, M. Liu, L.-B. Qu, X. Chen, L. Mi, *Chem. Mater.*, **2022**, 34, 5232–5240.
[25] J.-N. Chang, J.-W. Shi, Q. Li, S. Li, Y.-R. Wang, Y. Chen, F. Yu, S.-L. Li, Y.-Q. Lan, *Angew. Chem. Int. Ed.*, **2023**, 62, e202303606.
[26] C. Shu, X. Yang, L. Liu, X. Hu, R. Sun, X. Yang, A. I. Cooper, B. Tan, X. Wang, *Angew. Chem. Int. Ed.*, **2024**, 63, e202403926.
[27] Z. Xie, X. Chen, W. Wang, X. Ke, X. Zhang, S. Wang, X. Wu, J. C. Yu, X. Wang, *Angew. Chem. Int. Ed.*, **2024**, 63, e202410179.
[28] H. Yu, X. Zhang, Q. Chen, P.-K. Zhou, F. Xu, H. Wang, X. Chen, *Chem. Res. Chin. Univ.*, **2025**, 41, 734–740.
[29] C. Li, D. Li, W. Zhang, H. Li, G. Yu, *Angew. Chem. Int. Ed.*, **2021**, 60, 27135–27143.
[30] H. Yu, P.-K. Zhou, X. Chen, *Adv. Funct. Mater.*, **2023**, 33, 2308336.
[31] G. Ding, J. Zhao, K. Zhou, Q. Zheng, S.-T. Han, X. Peng, Y. Zhou, *Chem. Soc. Rev.*, **2023**, 52, 7071–7136.
[32] Q. Hao, X.-R. Ren, Y. Chen, C. Zhao, J. Xu, D. Wang, H. Liu, *Nat. Commun.*, **2023**, 14, 578.
[33] P. Zhou, H. Yu, M. Y. Chee, T. Zeng, T. Jin, H. Yu, S. Wu, W. S. Lew, X. Chen, *Chin. Chem. Lett.*, **2024**, 35, 109279.
[34] P.-K. Zhou, H. Yu, Y. Li, H. Yu, Q. Chen, X. Chen, *J. Polym. Sci.*, **2024**, 62, 1536–1553.
[35] P.-K. Zhou, Y. Li, T. Zeng, M. Y. Chee, Y. Huang, Z. Yu, H. Yu, H. Yu, W. Huang, X. Chen, *Angew. Chem. Int. Ed.*, **2024**, 63, e202402911.
[36] P.-K. Zhou, Y. Huang, Z. Yu, C. Zhang, Q. Chen, Y. Li, C. Lin, X. Chen, *Sci. China Chem.*, **2025**, 68, 3230–3237.
[37] J. Xu, C. Yang, S. Bi, W. Wang, Y. He, D. Wu, Q. Liang, X. Wang, F. Zhang, *Angew. Chem. Int. Ed.*, **2020**, 59, 23845–23853.
[38] W. Li, X. Huang, T. Zeng, Y. A. Liu, W. Hu, H. Yang, Y.-B. Zhang, K. Wen, *Angew. Chem. Int. Ed.*, **2021**, 60, 1869–1874.
[39] W. Zhang, L. Chen, S. Dai, C. Zhao, C. Ma, L. Wei, M. Zhu, S. Y. Chong, H. Yang, L. Liu, Y. Bai, M. Yu, Y. Xu, X.-W. Zhu, Q. Zhu, S. An, R. S. Sprick, M. A. Little, X. Wu, S. Jiang, Y. Wu, Y.-B. Zhang, H. Tian, W.-H. Zhu, A. I. Cooper, *Nature*, **2022**, 604, 72–79.
[40] H. Liu, D. Wang, Z. Yu, Y. Chen, X. Li, R. Zhang, X. Chen, L. Wu, N. Ding, Y. Wang, Y. Zhao, *Sci. China Mater.*, **2023**, 66, 2283–2289.
[41] Y.-N. Gong, X. Guan, H.-L. Jiang, *Coord. Chem. Rev.*, **2023**, 475, 214889.
[42] N. Liu, S. Xie, Y. Huang, J. Lu, H. Shi, S. Xu, G. Zhang, X. Chen, *Adv. Energy Mater.*, **2024**, 14, 2402395.
[43] L. Hao, R. Shen, C. Qin, N. Li, H. Hu, G. Liang, X. Li, *Sci. China Mater.*, **2024**, 67, 504–513.
[44] J. Liu, C. Tuo, W.-Y. Xiao, M.-Y. Qi, Y. Yusran, Z. Wang, H. Li, C. Guo, J. Song, S. Qiu, Y.-J. Xu, Q. Fang, *Angew. Chem. Int. Ed.*, **2025**, 64,

e202416240.
[45] A. Nagai, X. Chen, X. Feng, X. Ding, Z. Guo, D. Jiang, *Angew. Chem. Int. Ed.*, **2013**, 52, 3770–3774.
[46] X. Chen, M. Addicoat, E. Jin, L. Zhai, H. Xu, N. Huang, Z. Guo, L. Liu, S. Irle, D. Jiang, *J. Am. Chem. Soc.*, **2015**, 137, 3241–3247.
[47] L. Ma, S. Wang, X. Feng, B. Wang, *Chin. Chem. Lett.*, **2016**, 27, 1383–1394.
[48] Z. Li, Y. Zhi, P. Shao, H. Xia, G. Li, X. Feng, X. Chen, Z. Shi, X. Liu, *Appl. Catal. B*, **2019**, 245, 334–342.
[49] Z. Li, S. Han, C. Li, P. Shao, H. Xia, H. Li, X. Chen, X. Feng, X. Liu, *J. Mater. Chem. A*, **2020**, 8, 8706–8715.
[50] S. Ma, Z. Li, J. Jia, Z. Zhang, H. Xia, H. Li, X. Chen, Y. Xu, X. Liu, *Chin. J. Catal.*, **2021**, 42, 2010–2019.
[51] R. Sun, X. Hu, C. Shu, L. Zheng, S. Wang, X. Wang, B. Tan, *Chin. J. Catal.*, **2023**, 55, 159–170.
[52] Z. Luo, S. Zhu, H. Xue, W. Yang, F. Zhang, F. Xu, W. Lin, H. Wang, X. Chen, *Angew. Chem. Int. Ed.*, **2025**, 64, e202420217.
[53] X. Ding, L. Chen, Y. Honsho, X. Feng, O. Saengsawang, J. Guo, A. Saeki, S. Seki, S. Irle, S. Nagase, V. Parasuk, D. Jiang, *J. Am. Chem. Soc.*, **2011**, 133, 14510–14513.
[54] S. Tao, D. Jiang, *CCS Chem.*, **2021**, 3, 2003–2024.
[55] K.-T. Tan, S. Ghosh, Z. Wang, F. Wen, D. Rodríguez-San-Miguel, J. Feng, N. Huang, W. Wang, F. Zamora, X. Feng, A. Thomas, D. Jiang, *Nat. Rev. Methods Primers*, **2023**, 3, 1.
[56] X. Zeng, M. Guo, L. Wang, H. Xu, C. Lin, Z. Luo, F. Zhang, S. Zhu, S. Wang, Y. Fang, W. Lin, X. Chen, *Sci. Bull.*, **2025**, 70, 2725–2729.
[57] Z. Luo, X. Chen, W. Yang, Y. Chang, S. Zhu, F. Zhang, W. Lin, G. Xu, G.-E. Wang, X. Chen, *Sci. China Chem.*, **2025**, https://doi.org/10.1007/s11426–025–2781–4.
[58] Z.-A. Lan, G. Zhang, X. Chen, Y. Zhang, K. A. I. Zhang, X. Wang, *Angew. Chem. Int. Ed.*, **2019**, 58, 10236–10240.
[59] Z.-A. Lan, M. Wu, Z. Fang, X. Chi, X. Chen, Y. Zhang, X. Wang, *Angew. Chem. Int. Ed.*, **2021**, 60, 16355–16359.
[60] Z. Xie, W. Wang, X. Ke, X. Cai, X. Chen, S. Wang, W. Lin, X. Wang, *Appl. Catal. B*, **2023**, 325, 122312.
[61] Y. Qian, Y. Han, X. Zhang, G. Yang, G. Zhang, H.-L. Jiang, *Nat. Commun.*, **2023**, 14, 3083.
[62] R. Liu, M. Zhang, F. Zhang, B. Zeng, X. Li, Z. Guo, X. Lang, *Small*, **2025**, 21, 2411625.
[63] F. Zhang, Y. Wang, Q. Zhao, X. Dong, X.-K. Gu, H. Sheng, S. Sarina, X. Lang, *ACS Appl. Mater. Interfaces*, **2025**, 17, 1097–1109.
[64] M. Zhang, R. Liu, F. Zhang, H. Zhao, X. Li, X. Lang, Z. Guo, *J. Colloid Interface Sci.*, **2025**, 678, 1170–1180.
[65] C. Kaes, A. Katz, M. W. Hosseini, *Chem. Rev.*, **2000**, 100, 3553–3590.
[66] Z. Mi, T. Zhou, W. Weng, J. Unruangsri, K. Hu, W. Yang, C. Wang, K. A. I. Zhang, J. Guo, *Angew. Chem. Int. Ed.*, **2021**, 60, 9642–9649.
[67] H. Zhang, Z. Lin, P. Kidkhunthod, J. Guo, *Angew. Chem. Int. Ed.*, **2023**, 62, e202217527.
[68] Y. Shiraishi, S. Kanazawa, Y. Kofuji, H. Sakamoto, S. Ichikawa, S. Tanaka, T. Hirai, *Angew. Chem. Int. Ed.*, **2014**, 53, 13454–13459.
[69] W. Wang, H. Wang, X. Tang, J. Huo, Y. Su, C. Lu, Y. Zhang, H. Xu, C. Gu, *Chem. Sci.*, **2022**, 13, 8679–8685.
[70] Z. Xie, X. Yang, P. Zhang, X. Ke, X. Yuan, L. Zhai, W. Wang, N. Qin, C.-X. Cui, L. Qu, X. Chen, *Chin. J. Catal.*, **2023**, 47, 171–180.
[71] Z. Gu, Z. Shan, Y. Wang, J. Wang, T. Liu, X. Li, Z. Yu, J. Su, G. Zhang, *Chin. Chem. Lett.*, **2024**, 35, 108356.
[72] Z.-A. Lan, W. Ren, X. Chen, Y. Zhang, X. Wang, *Appl. Catal. B*, **2019**, 245, 596–603.
[73] G. Li, Z. Xie, S. Chai, X. Chen, X. Wang, *Appl. Catal. B*, **2021**, 283, 119637.
[74] G. Li, Z. Xie, Q. Wang, X. Chen, Y. Zhang, X. Wang, *Chem. Eur. J.*, **2021**, 27, 939–943.
[75] P. K. Zhou, C. Liang, C. Zhang, Y. Huang, Z. Yu, C. Lin, C. Zhang, Q. Sun, Y. Song, X. R. Ren, D. Wang, S. Wang, Y. M. Lam, X. Chen, *ACS Catal.*, **2025**, 15, 16992–17002.
[76] C. Li, H. Xu, H. Xiong, S. Xia, X. Peng, F. Xu, X. Chen, *Adv. Funct. Mater.*, **2024**, 34, 2405539.
[77] Y. Yu, C. Cao, H. Liu, P. Li, F. Wei, Y. Jiang, W. Song, *J. Mater. Chem. A*, **2014**, 2, 1677–1681.
[78] Y. Chen, B. Wang, S. Lin, Y. Zhang, X. Wang, *J. Phys. Chem. C*, **2014**, 118, 29981–29989.
[79] Y. Luo, B. Zhang, C. Liu, D. Xia, X. Ou, Y. Cai, Y. Zhou, J. Jiang, B. Han, *Angew. Chem. Int. Ed.*, **2023**, 62, e202305355.
[80] J.-N. Chang, Q. Li, J.-W. Shi, M. Zhang, L. Zhang, S. Li, Y. Chen, S.-L. Li, Y.-Q. Lan, *Angew. Chem. Int. Ed.*, **2023**, 62, e202218868.
[81] H. Yu, F. Zhang, Q. Chen, P.-K. Zhou, W. Xing, S. Wang, G. Zhang, Y. Jiang, X. Chen, *Angew. Chem. Int. Ed.*, **2024**, 63, e202402297.
[82] H. Xu, S. Xia, C. Li, Y. Li, W. Xing, Y. Jiang, X. Chen, *Angew. Chem. Int. Ed.*, **2024**, 63, e202405476.
[83] L. Chen, L. Wang, Y. Wan, Y. Zhang, Z. Qi, X. Wu, H. Xu, *Adv. Mater.*, **2020**, 32, 1904433.
[84] W. Zhao, P. Yan, B. Li, M. Bahri, L. Liu, X. Zhou, R. Clowes, N. D. Browning, Y. Wu, J. W. Ward, A. I. Cooper, *J. Am. Chem. Soc.*, **2022**, 144, 9902–9909.
[85] D. Chen, W. Chen, Y. Wu, L. Wang, X. Wu, H. Xu, L. Chen, *Angew. Chem. Int. Ed.*, **2023**, 62, e202217479.
[86] R. Liu, Y. Chen, H. Yu, M. Položij, Y. Guo, T. C. Sum, T. Heine, D. Jiang, *Nat. Catal.*, **2024**, 7, 195–206.
[87] H. Cheng, J. Cheng, L. Wang, H. Xu, *Chem. Mater.*, **2022**, 34, 4259–4273.
[88] D. Tan, R. Zhuang, R. Chen, M. Ban, W. Feng, F. Xu, X. Chen, Q. Wang, *Adv. Funct. Mater.*, **2024**, 34, 2311655.

联吡啶整合的双恶唑基给体-受体共价有机框架用于增强光催化过氧化氢合成

陆家平[a,b,1], 林　超[a,b,1], 李　超[c,1], 石泓杰[a,b], 刘能益[a,b], 邢万东[a,b,*], 汪思波[a,b,*], 张贵刚[a,b], 陈藤藤[c,*], 陈　雄[a,b,*]

[a]福州大学化学学院, 核生化灾害防护化学全国重点实验室, 福建福州350116
[b]福州大学化学学院, 能源与环境光催化国家重点实验室, 先进碳基功能材料福建省高校重点实验室, 福建福州350116
[c]香港科技大学化学系, 香港九龙999077

摘要: 过氧化氢(H_2O_2)作为一种环境友好且高效的氧化剂, 其全球需求持续增长. 然而, 工业上主流的蒽醌法制备H_2O_2存在高能耗和严重污染等问题. 光催化技术通过太阳能驱动氧气还原反应实现H_2O_2合成, 代表了一种绿色可持续的替代策略. 在众多光催化剂中, 共价有机框架(COFs)因其可调控的能带结构、高比表面积和规整的孔道结构而备受关注. 然而,

COFs中光生载流子复合快和分离效率低的问题制约了其光催化性能. 在COFs骨架中引入给体-受体(D-A)结构可有效抑制载流子复合, 并提升电荷分离效率. 此外, 联吡啶(Bpy)单元以其平面构型和富电子氮原子特性, 能够优化电子结构、扩展光响应范围并提供特定活性位点, 有望进一步提升COFs在光催化H_2O_2合成中的性能.

本研究旨在通过精确的分子设计, 构建新型D-A型COFs光催化剂, 并系统探究不同给体单元(尤其是Bpy单元)对光催化H_2O_2产生性能的调控机制. 选用4,4′,4″,4‴-(苯并[1,2-d:4,5-d′]双(恶唑)-2,4,6,8-四基)四苯胺(BBO-NH_2)作为共同的受体单元, 分别与联吡啶-5,5′-二甲醛(Bpy-CHO)和联苯-4,4′-二甲醛(Bph-CHO)通过席夫碱反应, 成功合成两种具有相同受体单元但不同给体模块的结晶性COFs, 分别命名为Bpy-COF和Bph-COF. 结构表征结果表明, 两种COFs均具备高结晶度、良好的热稳定性和介孔结构. 与Bph-COF相比, Bpy-COF得益于Bpy单元较小的分子内二面角, 表现出更高的比表面积和更强的亲水性. 更关键的是, Bpy单元的引入显著拓宽了材料的可见光吸收范围, 缩小了带隙, 并优化了能带位置. 在光催化性能评估中, Bpy-COF在纯水体系和H_2O/苯甲醇(BA)两相体系中的H_2O_2产率分别达1330和2570 μmol h^{-1} g_{cat}^{-1}, 远高于Bph-COF, 且其表观量子效率亦更优. 机理分析显示, Bpy-COF具有更低的激子结合能、更长的载流子寿命以及更优异的光电流响应和电荷分离效率, 这些因素协同提升了其光催化活性. 该优势源于Bpy单元增强的π共轭和D-A相互作用, 促进了层内和层间电荷传输. 原位漫反射红外傅里叶变换光谱和密度泛函理论计算进一步揭示了其反应路径: Bph-COF主要遵循两步单电子还原机制($O_2 \rightarrow \cdot OOH \rightarrow H_2O_2$), 而Bpy-COF中的Bpy单元因氮原子易质子化, 不仅强化了O_2的吸附, 还能通过形成1,4-内过氧化物中间体, 实现更高效的一步两电子还原路径, 从而确保H_2O_2的高效和高选择性合成.

综上, 本研究通过对比实验, 系统证实了在D-A型COFs中引入联吡啶给体单元的多重益处, 包括优化材料理化性质、促进光生电荷分离与传输, 以及提供独特活性位点等. 该工作为设计合成高性能COF光催化剂提供了新策略和深入的机理洞见. 展望未来, 基于杂原子掺杂的分子工程方法将在开发高效、稳定的光催化H_2O_2合成体系中发挥关键作用.

关键词: 共价有机框架; 给体-受体; 光催化; 生产过氧化氢; 氧还原反应

收稿日期: 2025-07-08. 接受日期: 2025-09-15. 上网时间: 2026-02-05.

*通讯联系人. 电子信箱: xwd@fzu.edu.cn (邢万东), sibowang@fzu.edu.cn (汪思波), tengtengchen@ust.hk (陈藤藤), chenxiong987@fzu.edu.cn (陈雄).

[1]共同第一作者.

基金来源: 国家重点研发计划(2021YFA1502100); 福建省自然科学基金(2024J01238); 国家自然科学基金(22572031、52201006和22172029)以及“111计划”(D16008); 香港科技大学启动基金(R9874); 青年科学家计划(26311224); 香港研究资助局普通研究基金(16312125); 中国科学技术协会青年精英科学家资助计划(2023QNRC001); 精密与智能化学重点实验室开放课题基金.